ACS Catalysis

pubs.acs.org/acscatalysis

Research Article

Does Cluster Encapsulation Inhibit Sintering? Stabilization of Size-Selected Pt Clusters on $Fe_3O_4(001)$ by SMSI

Sebastian Kaiser,[#] Johanna Plansky,[#] Matthias Krinninger, Andrey Shavorskiy, Suyun Zhu, Ueli Heiz, Friedrich Esch,[*] and Barbara A. J. Lechner[*]

Cite This: *ACS Catal.* 2023, 13, 6203–6213

Read Online

ACCESS | Metrics & More | Article Recommendations | Supporting Information

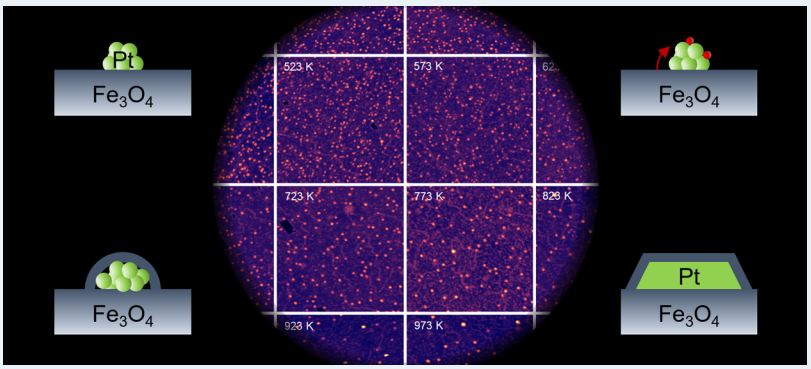

ABSTRACT: The metastability of supported metal nanoparticles limits their application in heterogeneous catalysis at elevated temperatures due to their tendency to sinter. One strategy to overcome these thermodynamic limits on reducible oxide supports is encapsulation via strong metal−support interaction (SMSI). While annealing-induced encapsulation is a well-explored phenomenon for extended nanoparticles, it is as yet unknown whether the same mechanisms hold for subnanometer clusters, where concomitant sintering and alloying might play a significant role. In this article, we explore the encapsulation and stability of size-selected Pt_5, Pt_{10}, and Pt_{19} clusters deposited on $Fe_3O_4(001)$. In a multimodal approach using temperature-programmed desorption (TPD), X-ray photoelectron spectroscopy (XPS), and scanning tunneling microscopy (STM), we demonstrate that SMSI indeed leads to the formation of a defective, FeO-like conglomerate encapsulating the clusters. By stepwise annealing up to 1023 K, we observe the succession of encapsulation, cluster coalescence, and Ostwald ripening, resulting in square-shaped crystalline Pt particles, independent of the initial cluster size. The respective sintering onset temperatures scale with the cluster footprint and thus size. Remarkably, while small encapsulated clusters can still diffuse as a whole, atom detachment and thus Ostwald ripening are successfully suppressed up to 823 K, i.e., 200 K above the Hüttig temperature that indicates the thermodynamic stability limit.

KEYWORDS: *size-selected clusters, strong metal−support interaction, sintering, encapsulation, heterogeneous catalysis, scanning tunneling microscopy, temperature-programmed desorption, X-ray photoelectron spectroscopy*

1. INTRODUCTION

To maximize material efficiency and to fully exploit non-scalable electronic effects in very small, subnanometer particles (called clusters) as heterogeneous catalysts, one has to counteract the intrinsic tendency of these metastable particles to sinter. Reducible oxides are both successful in stabilizing clusters and offer the possibility to exploit synergistic particle−support effects to tune catalytic activity and selectivity.[1,2] In terms of stabilization, adequate cluster binding sites at defects prevent cluster diffusion, while dewetting prevents atom diffusion.[3] Additionally, stabilization of particles by overgrowth of thin reducible oxide layers through the strong metal−support interaction (SMSI) effect has recently come into the focus of interest again.[4] The concept, first discussed by Tauster et al.,[5] holds for group VIII metals on reducible oxides and is well-established in ultrahigh vacuum (UHV) where an encapsulation layer, formed by reductive annealing, has been described as a reduced film of self-limiting thickness and defined stoichiometry for large nanoparticles and extended metal islands.[6,7] The stabilization of nanoparticles by SMSI effects has numerous implications in catalysis, ranging from methanol steam reforming,[8,9] over the water−gas shift reaction,[10] to low-temperature CO oxidation,[11] and the

Received: January 30, 2023
Revised: March 8, 2023
Published: April 21, 2023

https://doi.org/10.1021/acscatal.3c00448
ACS Catal. 2023, 13, 6203−6213

hydrogen oxidation reaction (HOR) under harsh oxidative conditions.[12,13] In terms of selectivity and activity tuning, SMSI has recently been invoked for its impact in CO_2 reduction, where the encapsulation suppresses methane in favor of CO formation in various catalytic systems.[14−16]

In real catalysts, the influence of SMSI can be observed as deactivation or change in selectivity,[1] but it is often challenging to differentiate it from sintering and to attribute it to a specific atomic-scale process, like particle encapsulation, or an electronic effect (for a recent example, see the article by Han et al.).[17] To disentangle the effects of SMSI and sintering, highly defined model systems—ideally with atomically defined particle sizes and controlled support stoichiometry—are required. For example, recent studies have shown that the growth of an encapsulation layer can be strongly dependent on pressure conditions[18] and on steady-state redox dynamics.[19] In this context, many questions still remain, particularly pertaining to the growth dynamics of the film, its permeability to diffusion of small reactants, and the stability of the encapsulated particles. To date, the encapsulation phenomenon by SMSI has only been investigated for nanoparticles, but its extension to the subnanometer scale is still a largely unexplored territory. Specifically, the small cluster footprint strongly facilitates cluster diffusion in the temperature regimes where encapsulation takes place. Atomically resolving microscopy combined with highly sensitive reactivity measurements provides unmatched insights into encapsulation and sintering processes on the atomic scale, allowing us to discern whether the clusters remain size-selected or might even be completely integrated into the substrate. Such dynamic effects are increasingly discussed in the literature in the context of single-atom versus cluster catalysis[20] and potential interchange between the two.[21−23] In our research, we study the cluster encapsulation and concomitant sintering behavior on the atomic scale with sound statistics and across a wide temperature range, with the aim to enable heterogeneous catalysis at stabilized subnanometer particles under harsh conditions.

Clusters have been shown to exhibit various exciting size effects that can be exploited for their catalytic activity, in the extreme case leading to drastic changes in turnover frequencies with the addition or removal of just a single atom to/from the cluster.[24,25] As a consequence, where sintering control is already a key issue in nanoparticle catalysts, it is even more crucial when it comes to stabilizing specific cluster sizes. Two distinct sintering mechanisms have been described, Ostwald and Smoluchowski ripening.[3,26−28] Ostwald ripening is particle coarsening by detachment of single atoms, which diffuse and reattach to other particles.[29] While the maximum onset temperature depends on the particle material and can be estimated by the so-called Hüttig temperature, where atoms start to detach from undercoordinated sites,[30,31] smaller particles (i.e., those with a high curvature) such as clusters exhibit a higher vapor pressure and thus start to sinter much earlier.[32] This curvature dependence generally leads to particles of larger diameter growing at the expense of smaller ones. Smoluchowski ripening, on the other hand, is sintering by migration of entire particles and coalescence with neighboring ones, yielding only multiples of the original cluster size.[33] While Ostwald ripening critically depends on the atom detachment energy, the onset temperature for Smoluchowski ripening is determined by the strength of the particle−support interaction influencing the diffusion energy barrier, which scales approximately with the cluster footprint, typically resulting in an atom-by-atom size dependence.[34]

To date, various approaches to particle stabilization have been suggested. For subnanometer clusters, it has been shown that size selection alone can kinetically mitigate Ostwald ripening.[35] However, theoretical calculations suggest that sintering can indeed be accelerated in cluster sizes that exhibit a large number of isomers that fluxionally interconvert.[36] Other stabilization methods such as alloying with stabilizing metals[37,38] or increasing the particle distance by use of high-surface-area supports[39] have been shown to successfully prevent particle sintering. Last but not least, particle redispersion strategies have been presented as alternatives for reactivating catalysts.[23] Here, we follow the stabilization approach via SMSI as a pathway that maintains cluster size selection and hence the potential to fully control catalyst activity.

In the present work, we investigate the encapsulation and sintering of size-selected Pt_{5-19} clusters deposited on a magnetite, $Fe_3O_4(001)$, support. Iron oxides are abundant materials that exhibit a rich redox chemistry,[40] and magnetite in particular is magnetic, reducible, and conductive. It crystallizes in an inverse spinel structure, whereby the O^{2-} anions form an fcc lattice with Fe^{2+} occupying octahedral sites and Fe^{3+} tetrahedral and octahedral sites in a 1:1 ratio.[41−43] The $Fe_3O_4(001)$ surface reconstructs into the subsurface cation vacancy (SCV) reconstruction, yielding a $(\sqrt{2} \times \sqrt{2})R45°$ structure with only Fe^{3+} occupying the uppermost layers.[44] This reconstruction can be observed as parallel, undulating rows in scanning tunneling microscopy (STM), which are rotated by 90° between two adjacent atomic terraces. The (001) surface exhibits a variety of different defects,[45−48] which can participate in its surface chemistry as adsorption and dissociation sites for molecules.[49−52] Moreover, we have recently shown that lattice oxygen from the magnetite support can readily participate in catalytic reactions by migrating onto Pt clusters, which we termed lattice oxygen reverse spillover.[53] Here, we use temperature-programmed desorption (TPD), high-resolution synchrotron X-ray photoelectron spectroscopy (XPS), and STM measurements to show the formation of an encapsulating SMSI layer even on these small clusters, investigate its redox state and morphology, and clarify the sintering mechanism for Pt_5, Pt_{10}, and Pt_{19} clusters, where we pinpoint the cluster size-dependent onset of Smoluchowski ripening and subsequently that of Ostwald ripening.

2. EXPERIMENTAL METHODS

Natural $Fe_3O_4(001)$ crystals (SurfaceNet GmbH) were prepared by a series of cleaning cycles, each consisting of Ar^+-ion bombardment (20 min, 4×10^{-5} mbar Ar, 1 keV, 5.0 μA sputter current) and subsequent annealing in an oxygen atmosphere (20 min, 5×10^{-7} mbar O_2, 983 K). The reproducibility of the preparation procedure and the cleanliness and stoichiometry of the crystals were checked regularly by STM and XPS. Size-selected Pt clusters were generated using a laser ablation cluster source.[54] Here, the second harmonic of a Nd:YAG laser is used to evaporate Pt from a rotating target, yielding a plasma, which is subsequently cooled in the adiabatic expansion of a He pulse (Westfalen AG, grade 6.0), resulting in a broad distribution of clusters. A series of electrostatic lenses guides the clusters toward a 90° bender for charge selection, followed by a quadrupole mass filter for

https://doi.org/10.1021/acscatal.3c00448
ACS Catal. 2023, 13, 6203−6213

size selection. Finally, the clusters are deposited onto the substrate under soft landing conditions (kinetic energy <1 eV/atom). For all experiments, cluster deposition was carried out at room temperature. A cluster coverage of 0.05 clusters/nm^2 was deposited.

The TPD and STM measurements were performed under UHV conditions, with a system base pressure of <1 × 10^{-10} mbar. Temperature control is performed with the same sample holder for all experiments, using a pyrolytic boron nitride heater located directly below the sample and a type K thermocouple in direct contact with the sample, with an absolute estimated accuracy of ±5 K. All TPD experiments were carried out using the sniffer, a mass spectrometer-based (Pfeiffer Vacuum GmbH, QMA 200 Prisma Plus) reactivity measurement device, designed for high sensitivity measurements of low-coverage cluster samples.[55] To maximize the signal and ensure a low signal-to-noise ratio, all TPD-related samples have been saturated with C^{18}O (Eurisotop, 96.1%) already during cluster deposition.

The STM measurements were performed in constant current mode with a commercial Scienta Omicron VT-AFM instrument, using homemade etched W tips. To disentangle time and temperature effects, we systematically annealed the sample for 10 min in 50 K steps before measuring the resulting cluster distribution at room temperature. The STM images were processed with Gwyddion using the plane subtraction and row-by-row alignment tools for background correction.[56] The height distribution of the particles was determined using a home-written Igor routine, by detecting the particles via an intensity threshold, drawing a profile through the cluster maximum, and determining the height of the cluster with respect to the median background of the image. For higher statistical significance, the cluster heights of ten 100 × 100 nm^2 STM images were used, recorded both in the center and at the edge of the sample for each annealing temperature. A minority of clusters which were located at step edges, at the edge of the image, or in small holes were excluded from the height analysis but included in the coverage determination. In images with more than one terrace, a separate evaluation was carried out for each terrace.

High-resolution XPS measurements were performed at the APXPS endstation of the HIPPIE beamline,[57] MAX IV laboratory in Lund, Sweden, which is equipped with a Scienta Omicron HiPP-3 electron energy analyzer. A homebuilt UHV suitcase with a base pressure of ∼1 × 10^{-10} mbar was used for sample transfer after cluster deposition in our laboratories in Munich to the beamline in Lund, ensuring clean, intact and still size-selected cluster samples. To desorb any adsorbates accumulated during the several-day-long transport in the UHV suitcase (presumably mainly CO and traces of hydrocarbons), we started the experiment by heating the sample to 373 K to desorb the adsorbates. This resulted in a shift of 0.6 eV to lower binding energies, corresponding to CO desorption,[58,59] and a reduction of the peak width for the Pt 4f signal, and no clear shift in the Fe 3p (compare Figure S1). For heating, an infrared laser directly illuminating the back of the sample was used. The temperature was measured with a type K thermocouple mounted to the side of the crystal. Below, we indicate the temperatures as measured, which could be somewhat underestimated due to limited heat transfer. The XP spectra were acquired in UHV with photon energies of 307 and 921 eV and a constant pass energy and emission angle (normal emission). Initial checks showed no significant beam damage, thus we recorded all spectra at the same spot on the sample (i.e., with the same cluster coverage) to allow quantitative comparison of the spectra. In data evaluation using KolXPD,[60] the binding energies were calibrated with respect to the Fermi edge and all spectra normalized to their low-binding-energy background. A Shirley background was subtracted from the spectra before quantitative analysis.

3. RESULTS AND DISCUSSION

3.1. Encapsulation of Subnanometer Clusters Induced by Strong Metal−Support Interaction. To investigate whether and how SMSI influences cluster sintering dynamics, we first need to establish that encapsulation of clusters actually occurs. In our recent work on lattice oxygen reverse spillover on Pt/Fe_3O_4(001), we have already found first indications for cluster encapsulation in our TPD experiments, namely, the loss of CO adsorption sites and thus CO_2 formation capability upon heating beyond a certain temperature threshold.[53] We now investigate this phenomenon in more detail on the example of Pt_{19}, by TPD and high-resolution XPS, focusing on the exact growth conditions, redox state, and morphology of the encapsulating layer, starting with the CO TPD from our previous work (compare Figure 1, first run).

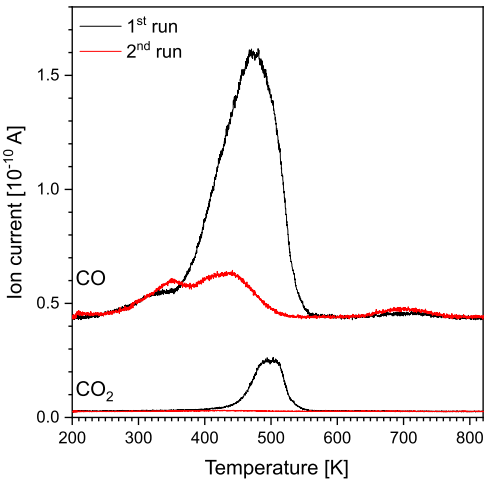

Figure 1. Two subsequent CO TPD spectra of Pt_{19} clusters supported on Fe_3O_4(001) recorded after exposing the sample to a saturating amount of C^{18}O at 200 K (∼10 L) before each run. The C^{18}O (m/z = 30, top, offset for clarity) and C^{18}O^{16}O (m/z = 46, bottom) traces are shown. The heating rate was 1 K/s. A clear loss of the main desorption feature in the second run can be observed for both traces, with new, lower temperature features appearing in the CO trace, which hint at the presence of FeO defect sites. Furthermore, the CO_2 production is completely suppressed in the second run.

The main CO desorption feature in the first run (black), with a peak at 475 K, arises from desorption from the clusters, as it is not observed on the clean magnetite surface (see Figure S2).[50,53] The rather weak, broad feature around 700 K, in contrast, belongs to recombinative desorption of CO from reduced Fe sites such as Fe adatoms.[46,61] In the second TPD run (red), the main CO desorption peak has vanished completely and instead two new, overlapping and less intense desorption features with maxima at 350 and 430 K emerge. Indeed, the new CO desorption features appearing in the second TPD are comparable to literature spectra from oxygen

https://doi.org/10.1021/acscatal.3c00448
ACS Catal. 2023, 13, 6203−6213

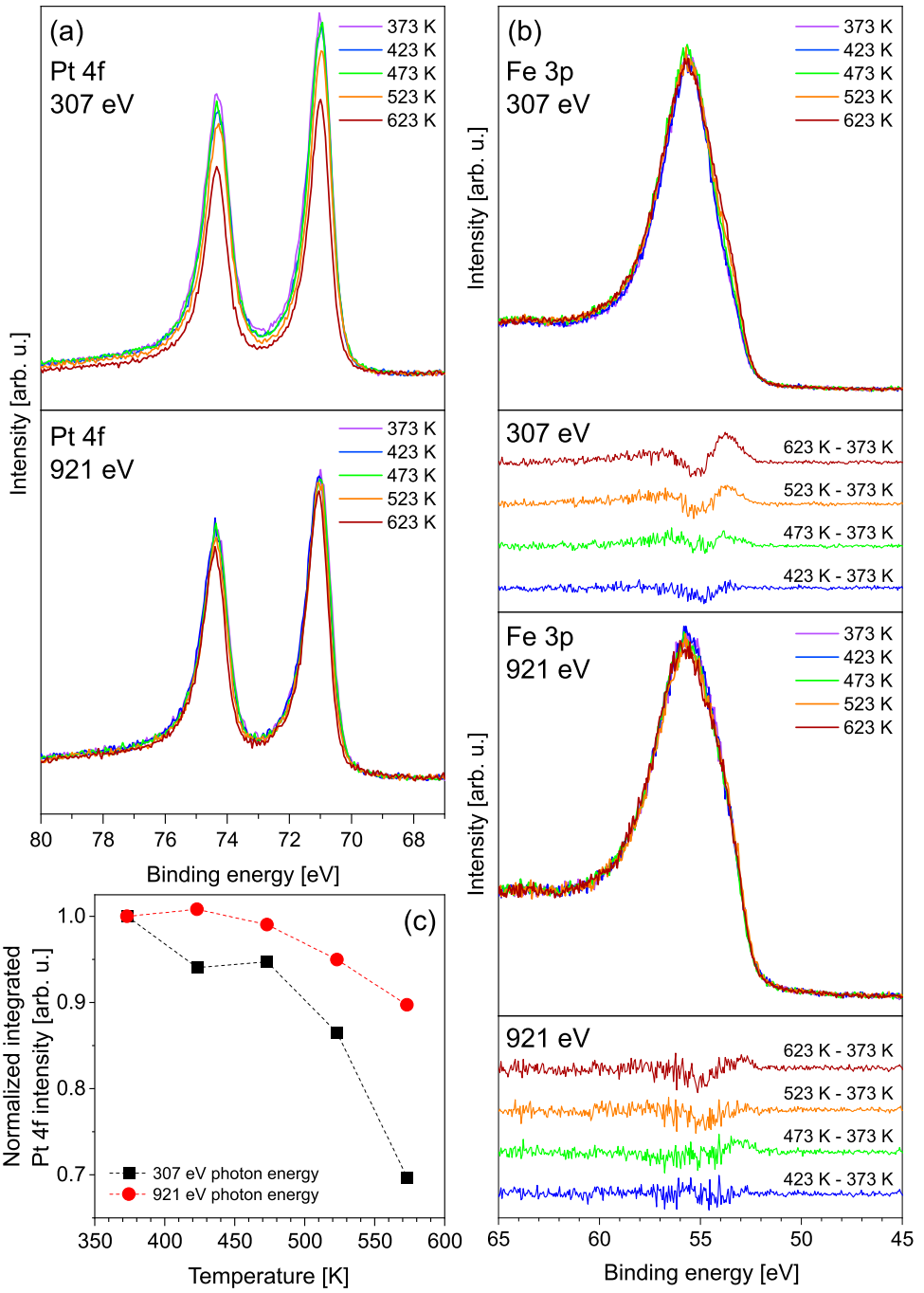

Figure 2. XP spectra of $Pt_{19}/Fe_3O_4(001)$ (0.05 clusters/nm^2) measured at 307 eV (highly surface-sensitive) and 921 eV photon energy (more bulk-sensitive), at the indicated temperatures in UHV. (a) Pt 4f spectra and (b) Fe 3p spectra with corresponding difference spectra for each photon energy below. (c) Evolution of the Pt 4f integrals for each photon energy, scaled to the first spectrum, respectively.

vacancy defect sites on FeO films.[62] Additionally, the desorption peak at 700 K has increased significantly in intensity compared to the first TPD run, again hinting at a more reduced surface which is in perfect agreement with an SMSI encapsulation state similar to that described for Pt nanoparticles on different magnetite facets.[7,63] Control measurements via STM showed that these TPD runs are ramped quickly enough that sintering is still avoided.[53]

Concurrently with the CO desorption, CO_2 formation is observed as a broad feature in the first TPD run, originating from catalytic CO oxidation with lattice oxygen,[53] which is completely lost in the second run. When dosing the same quantity of clusters on top of the already heated sample, the same signal reappears in the first run after redeposition and disappears again in a second run (see Figure S2). Importantly, the resulting FeO defect-related peak intensity scales with Pt cluster coverage, indicating the formation of reduced iron oxide in the vicinity of the clusters. Since magnetite is known to maintain its surface stoichiometry upon surface reduction by cation diffusion into the bulk,[64−66] those reduced FeO species must be located *on* the clusters, rather than around them, which is direct evidence for an SMSI effect. Note that due to the small cluster size, a stoichiometric, crystalline encapsulating layer, as observed for nanoparticles, is unlikely. The adsorption

https://doi.org/10.1021/acscatal.3c00448
ACS Catal. 2023, 13, 6203−6213

sites at the cluster surface are more likely blocked by a conglomerate of iron and oxygen atoms of unknown structure and stoichiometry that is hardly distinguishable from a Pt−FeO alloy.

To further confirm the encapsulation, we subsequently softly sputtered an encapsulated cluster sample, whereby indeed the encapsulating layer could be partially removed (restoring some of the original CO adsorption sites) and lost again during another TPD (see Figure S3). This particular encapsulation state is thus reproducibly obtained during a heating ramp to 820 K.

To sum up, the TPD experiments strongly indicate that the clusters get encapsulated by iron oxide upon annealing as a consequence of SMSI, whereby the desorption feature assignment indicates iron cations in a reduced state. We find that the loss in CO adsorption sites and hence cluster encapsulation also holds true for Pt_5 and Pt_{10} (see Figure S4).

To confirm the presence of reduced FeO and the encapsulation of Pt clusters, we performed high-resolution synchrotron XPS measurements on $Pt_{19}/Fe_3O_4(001)$, shown in Figure 2. We start by evaluating the attenuation of the Pt 4f signal induced by the encapsulating layer, comparing highly surface- and more bulk-sensitive measurements, recorded at 307 and 921 eV photon energy, respectively. Figure 2a displays the Pt 4f region measured at the indicated temperatures between 373 and 623 K. The binding energy remains unchanged, but upon increasing the temperature, a significant decrease in intensity is observed starting around 523 K in the surface-sensitive spectra (top panel), whereas the more bulk-sensitive spectra change much less significantly (bottom panel). This effect is quantified in Figure 2c, where the XP spectra from Figure 2a are integrated and for each photon energy normalized to the corresponding 373 K spectrum. Evidently, the Pt 4f signal decrease is more pronounced for the surface-sensitive measurement, as expected for an SMSI-induced encapsulation of clusters, thus confirming our interpretation of the TPD experiments and ruling out evaporation of Pt into the gas phase. A dissolution or diffusion of the clusters into the bulk, on the other hand, can be excluded by the only slightly decreasing Pt 4f signal in the more bulk-sensitive measurement at 921 eV photon energy, as well as by the STM measurements (discussed below), which is consistent with previous reports in the literature where neither Pt atoms nor clusters can be incorporated in bulk magnetite.[20,65,67] This experiment already gives insights into the morphology of the encapsulating layer. Although alloying cannot be excluded entirely, the reduction of the signal intensity indicates an additional layer on top of the clusters, which is also in line with the sputtering experiment described above. Modeling the attenuation by an FeO encapsulating layer, a nominal average thickness of about 2.2 Å can be calculated,[46,68−71] comparable to the 2.5 Å for a bilayer in bulk FeO.[72] These findings agree well with those reported for larger Pt nanoparticles on $Fe_3O_4(111)$, where the encapsulating layer has been identified as an FeO bilayer under UHV conditions.[73]

Figure 2b shows the Fe 3p XPS region measured at the indicated temperatures. In the main peak, no significant change is observed for either photon energy, suggesting that the support overall remains unchanged upon heating. Cluster-related changes in the Fe 3p signal are expected to be minimal due to the low coverage. Indeed, we observe the development of a small low-binding-energy shoulder in the Fe 3p region measured with 307 eV photon energy, in the same temperature range in which the decrease of the Pt 4f signal occurs. Fitting these peaks is not trivial,[74,75] and minimal changes can be overlooked easily. We instead use the difference spectra to interpret the data, as shown in Figure 2b for both photon energies. Here, in the more surface-sensitive spectra the shoulder is apparent as a peak around 53.8 eV that increases in intensity when the temperature is increased beyond ∼500 K. We assign this peak to Fe^{2+}.[74] At the same time, the signal corresponding to Fe^{3+}, at around 55.2 eV, decreases in intensity.[74] For the more bulk-sensitive measurement at 921 eV photon energy, the observed changes are in principle the same, but the intensity differences are significantly lower. Note that these transformations occur well below the known phase transition temperature of magnetite (001) around 720 K.[64] Thus, a slight increase in the Fe^{2+} content on the surface can be deduced, which we assign to the encapsulating SMSI layer, since all major changes in the Fe 3p signal develop around the same temperature where the highest decrease in the Pt 4f signal is observed. In agreement with our interpretation of the TPD experiments, the encapsulating layer on subnanometer clusters thus consists of reduced iron oxides, presumably FeO-like, similar to that around larger nanoparticles. The appearance of the encapsulating Fe^{2+} species is not necessarily a direct transformation of surface-Fe^{3+} species, but rather an extraction of interstitials to form the encapsulation layer. Indeed, DFT calculations showed that surface-Fe^{3+} extraction and subsequent adsorption on a Pt cluster is rather energy intensive.[53]

Summarizing, our TPD and XPS experiments confirm for the first time that encapsulation induced by SMSI indeed occurs also for subnanometer clusters and not only for extended nanoparticles and islands. We could identify the encapsulating layer as reduced defect-rich iron oxide, which covers the clusters.

3.2. Cluster-Size-Dependent Sintering Mechanisms.

Having established encapsulation of Pt clusters, we now proceed to investigating how cluster sintering occurs under the SMSI conditions identified above. In particular, we investigate which ripening mechanisms occur, whether the cluster size plays a role, and what the sintered particles look like. Pt_5, Pt_{10}, and Pt_{19} clusters on $Fe_3O_4(001)$ were deposited with similar cluster coverages at room temperature and subsequently annealed to increasingly higher temperatures in 50 K steps. Figure 3 shows representative STM images at the temperatures where the most significant changes occur (for a complete set of images see Figures S5−S7), while a detailed height profile analysis of 10 images at each temperature and cluster size is given in Figure 4 (the complete set of height histograms is shown in Figures S8−S10). The clusters appear as bright protrusions in STM images, while the atomic-scale contrast and defects of the magnetite surface are also visible with a lower corrugation. Even though STM cannot distinguish individual atoms within the cluster, we can exclude the presence of single-atom species like those reported previously.[67] We investigate four main temperature ranges in turn below, which we will relate to as-deposited size-selected clusters, lattice oxygen reverse spillover and encapsulation, cluster diffusion (Smoluchowski ripening), and Ostwald ripening.

As evidenced by the STM images in Figure 3a−c and corresponding height profiles in Figure 4, the as-deposited clusters are indeed size-selected, intact, and randomly distributed on the surface. To give a reference for cluster

https://doi.org/10.1021/acscatal.3c00448
ACS Catal. 2023, 13, 6203−6213

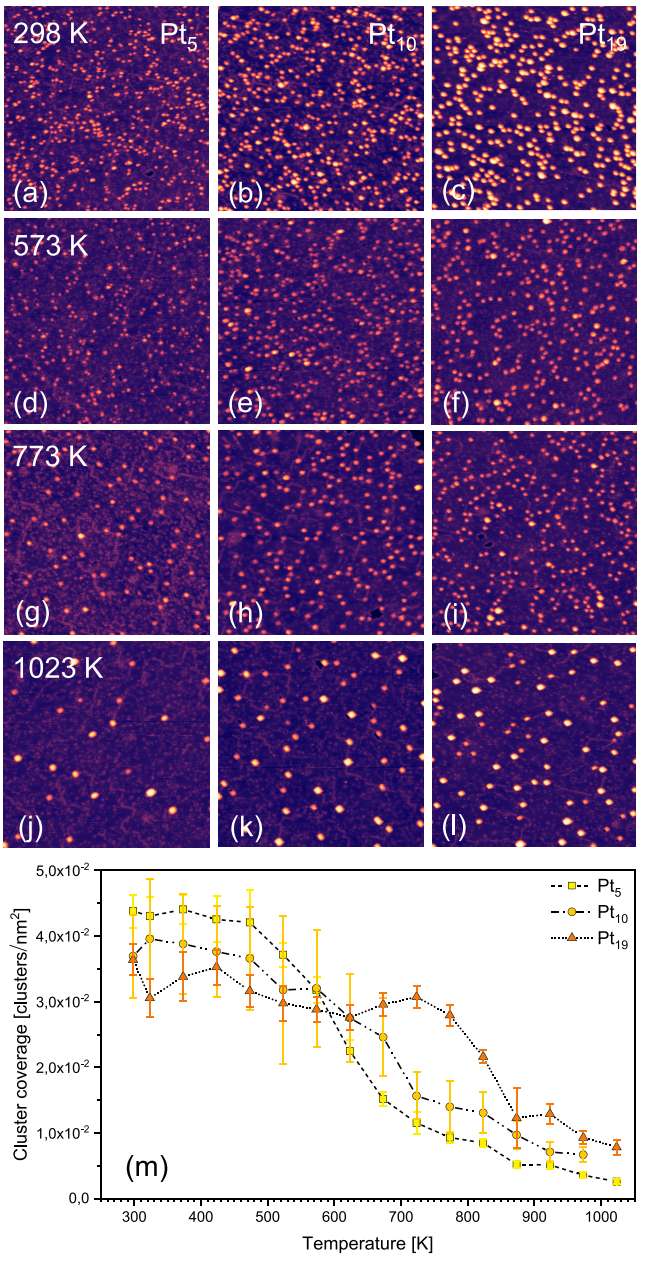

Figure 3. STM images of Pt_5 (left), Pt_{10} (center), and Pt_{19} (right column) clusters on $Fe_3O_4(001)$ (~0.05 clusters/nm^2) are shown (a–c) as-deposited, after annealing for 10 min each to (d–f) 573 K, (g–i) 773 K, and (j–l) 1023 K. For height comparison, all images use the same color scale. Imaging conditions: 1.5 V, 300 pA, 100 × 100 nm^2, and RT. (m) Cluster coverage as a function of temperature, extracted from ten 100 × 100 nm^2 images for each condition and cluster size, leading to an initial number of ~5000 clusters contributing to the evaluation.

layering, we can use the height distributions and compare them with the bulk Pt(111) step height of about 2.26 Å,[76] while keeping in mind that clusters typically have non-fcc structures and their apparent heights are influenced by electronic effects. The as-deposited Pt_5 clusters exhibit a height distribution with a single clear peak between one and two atomic layers. In contrast, the distribution for Pt_{10} clusters has a double peak around two and 2.5 layers and Pt_{19} clearly displays at least three separate heights, with a most common apparent height between three and four atomic layers. The different apparent cluster heights within each cluster size distribution are due to structural isomers and various adsorption sites on the surface.

When annealing up to 423 K, no significant changes are observed in the coverage nor height profiles for all three cluster sizes. In the temperature window from 473 to 573 K (see the Supporting Information), a decrease in apparent height is observed for all cluster sizes, which reaches a minimum after annealing to 623 K, yielding approximately single-layer Pt_5 and Pt_{10} clusters and Pt_{19} between one and two layers. Note that the cluster coverage initially remains unchanged but begins to drop for Pt_5 and Pt_{10} due to cluster-diffusion-induced sintering at cluster-footprint-dependent onset temperatures, as seen in Figures 3m and S8–S10. As we described previously, the initial height decrease of the clusters results from lattice oxygen reverse spillover.[53] Furthermore, as shown above, the clusters become encapsulated by the reduced FeO layer in the same temperature range where a semiconductor-like conductivity has been described for encapsulated Pt nanoparticles on $TiO_2(110)$.[6] Such a change in the electronic nature of the particle can additionally affect the imaging and therefore also contribute to the observed decrease in apparent height.

For Pt_5 and Pt_{10} clusters, the apparent cluster height increases again upon further annealing to 773 K, coinciding with a pronounced decrease in coverage due to sintering. With each temperature step, the coverage decreases further, until 773 K, where the curve flattens again. At the same time, the coverage and height distribution for Pt_{19} clusters remains unchanged, i.e., the clusters are still size-selected. Notably, for all three initial cluster sizes, the height distributions now have a similar width predominantly between one and 2.5 layers. The sinter resistance of the larger Pt_{19} combined with the similar resulting height distributions for all three initial sizes is clear evidence for Smoluchowski ripening, i.e., sintering by cluster diffusion. The diffusion barrier for clusters scales with their footprint and thus their interaction with the support.[34] Our data indicates that all Pt_{19} isomers have a footprint large enough to be stabilized against diffusion in this temperature regime, which is why the sintering process of the smaller clusters naturally terminates when all clusters reach this size range. Therefore, already the coalescence of two Pt_{10} or four Pt_5 clusters is sufficient to immobilize the resulting particles which makes the formation of larger nanoparticles statistically unlikely. Consequently, a narrow size distribution without much larger particles at this point is expected even after sintering, which is exactly what is observed in Figures 3g–i and 4. As the coverage curve in Figure 3m demonstrates, the Pt_5 clusters begin to sinter at 523 K, i.e., 100 K before Pt_{10}, another strong indication for footprint dependence. Remarkably, we thus observe that even encapsulated clusters can still diffuse across the surface, substantiating our hypothesis that an Fe–O agglomerate covers the clusters rather than a stoichiometric, rigid film.

By further increasing the temperature to 823 K, the situation changes. For all three investigated cluster samples, of which only the Pt_{19} clusters were still size-selected up to 773 K, a peak at lower heights of about one atomic layer grows in Figure 4, indicating a relatively larger proportion of smaller clusters. When annealing further to 873 K, this peak dominates the spectrum. Additionally, weak peaks at three and four atomic layers start to appear, implying the formation of larger particles. This observation of diverging cluster sizes is typical for Ostwald ripening, where larger particles grow at the expense of smaller ones that exhibit a higher vapor pressure.[32]

https://doi.org/10.1021/acscatal.3c00448
ACS Catal. 2023, 13, 6203–6213

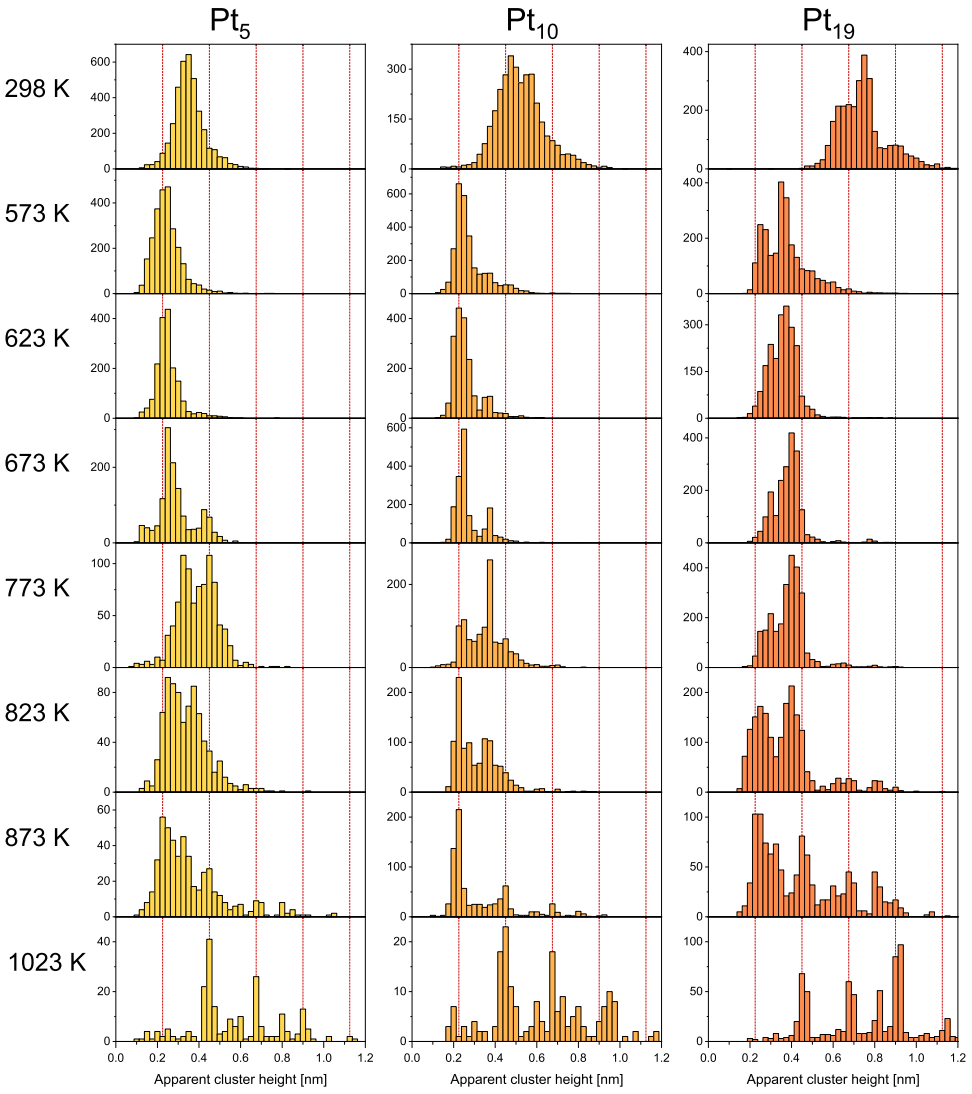

Figure 4. Histograms showing height distributions of Pt_5, Pt_{10}, and Pt_{19} clusters on $Fe_3O_4(001)$ for different selected annealing temperatures. Absolute cluster numbers are indicated on the *y*-scale. For each temperature and cluster size, an area of 100 000 nm^2 was analyzed (corresponding to the same data used in Figure 3m). To guide the eye, we added red dotted lines in bulk Pt(111) step increments.

Further increasing the temperature to 1023 K, the now strongly sintered particles are mainly two to four atomic layers in height, with a small number being one or five layers high. At the same time, the coverage has decreased yet again for each initial cluster size. The particles formed at this final temperature adopt a square shape aligned with the cubic symmetry of the underlying support (Figure 3 and details enlarged in Figure S11) and have sharp apparent heights which can be clearly assigned to atomic layers, comparable to the results observed for atomic Pt deposition and sintering on the same support.[63] We enter a size regime where we start to have a clear crystalline-like layering while the internal atom arrangement and thus the overall particle shape are still dominated by the support registry. From the resulting particle coverage and size distribution, and taking into account the initially deposited amount of Pt, we roughly estimate that most particles contain between 50 and 150 atoms.

We have thus shown that both Smoluchowski and Ostwald ripening occur for size-selected Pt clusters on $Fe_3O_4(001)$, whereby the mechanism strongly depends on the cluster size. Smaller clusters sinter via coalescence up to a size where the increasing diffusion barrier starts to be larger than that for atom detachment and Ostwald ripening dominates. Experimentally, it is impossible in this system to investigate sintering of the bare clusters since encapsulation occurs in a similar temperature window. Theoretical calculations for a comparable system, namely, Pd clusters on $CeO_2(111)$ indicate a similar effect.[34] There, Smoluchowski ripening is only possible for Pd_4 or smaller, whereas larger clusters sinter via Ostwald ripening.

As mentioned in Section 1, sintering of clusters via Ostwald ripening invariably begins at the empirical Hüttig temperature at the latest,[3,37] which is related to the melting point of the respective particle material and has been reported to be 608 K for Pt.[30] The actual onset temperature depends on the interaction with the support that influences the atom detachment energy. For unselected Pt clusters on Si_3N_4 films, for example, it has been shown that cluster sintering already sets in at 453 K.[35] In contrast, we observe Ostwald ripening of Pt on $Fe_3O_4(001)$ starting at a temperature of 823 K, which is roughly 200 K *above* the Hüttig temperature, indicating a strong stabilization against sintering beyond the thermodynamic limit. With the strong experimental evidence

https://doi.org/10.1021/acscatal.3c00448
ACS Catal. 2023, 13, 6203−6213

for an encapsulating SMSI layer described above, we conclude that the clusters are stabilized by encapsulation. While the encapsulating layer clearly mitigates Ostwald ripening, the smallest clusters can still diffuse even when covered with an FeO-like conglomerate, leading to Smoluchowski ripening. The observation of moving encapsulated particles is in contrast to the recent literature, where an SMSI layer stabilizes Pt nanoparticles on titania against migration.[19]

4. CONCLUSIONS

In the present work, we have investigated the stability of small size-selected Pt clusters deposited on $Fe_3O_4(001)$ to elucidate the strong metal−support interaction (SMSI) for catalytically active particles in the nonscalable size regime. Combined XPS and TPD experiments give clear evidence for the occurrence of encapsulation of subnanometer clusters. While the cluster surface is no longer accessible for CO adsorption, increased desorption from reduced iron oxide species points toward the formation of a defective FeO-like species encapsulating the clusters. Indeed, we observe the formation of a cluster-related Fe^{2+} species, concomitant to an attenuation of the Pt 4f signal.

For a precise analysis of the cluster stability, we performed STM studies of Pt_5, Pt_{10}, and Pt_{19}, starting from comparable cluster coverages and annealing stepwise to 1023 K. The evolution of cluster coverage and apparent height indicates successive cluster coalescence (Smoluchowski) and Ostwald ripening regimes, with a transition temperature that strongly depends on the cluster footprint and thus on the initial cluster size. The final particle distribution appears to be independent from the initial cluster size and overall deposited Pt atom coverage, and shows square particle shapes with well-defined layer heights.

Remarkably, both sintering mechanisms are observed despite the encapsulation. That being said, Ostwald ripening sets in at an unexpectedly high temperature of 823 K, i.e.,200 K above the Hüttig temperature. We therefore conclude that the encapsulating layer strongly stabilizes the clusters against atom detachment while still initially allowing diffusion of the smallest clusters. As one might expect for particles close to the atomic limit of the size regime, all our observations point to an encapsulating layer that is rather a conglomerate of Fe and O atoms surrounding the clusters than a stoichiometric, rigid iron oxide layer. It remains to be shown how the encapsulating layer changes in composition and morphology while clusters diffuse and coalesce, decay, and grow. With our experimental approach, we provide a new route to investigating model catalysts on the atomic scale to pave the way toward controlled use of SMSI for highly selective and sinter-resistant cluster catalysts in real heterogeneous catalysis.

■ ASSOCIATED CONTENT

Supporting Information

The Supporting Information is available free of charge at https://pubs.acs.org/doi/10.1021/acscatal.3c00448.

XP spectra including as-deposited measurements and desorption of adsorbates (S1); additional Pt_{19} deposition on already encapsulated $Pt_{19}/Fe_3O_4(001)$ (S2); partial removal of SMSI-induced layer by soft sputtering (S3); subsequent CO TPDs for Pt_5 and Pt_{10} clusters on $Fe_3O_4(001)$ (S4); representative STM images for all annealing temperatures for Pt_5, Pt_{10}, and Pt_{19} clusters on $Fe_3O_4(001)$ (S5); cluster height distributions for all annealing temperatures for Pt_5, Pt_{10}, and Pt_{19} clusters on $Fe_3O_4(001)$ (S6); and sintered Pt nanoparticles on $Fe_3O_4(001)$ (S7) (PDF)

■ AUTHOR INFORMATION

Corresponding Authors

Friedrich Esch − *Chair of Physical Chemistry and Catalysis Research Center, Department of Chemistry, School of Natural Sciences, Technical University of Munich, 85748 Garching, Germany;* orcid.org/0000-0001-7793-3341; Email: friedrich.esch@tum.de

Barbara A. J. Lechner − *Functional Nanomaterials Group and Catalysis Research Center, Department of Chemistry, School of Natural Sciences, Technical University of Munich, 85748 Garching, Germany; Institute for Advanced Study, Technical University of Munich, 85748 Garching, Germany;* orcid.org/0000-0001-9974-1738; Email: bajlechner@tum.de

Authors

Sebastian Kaiser − *Chair of Physical Chemistry and Catalysis Research Center, Department of Chemistry, School of Natural Sciences, Technical University of Munich, 85748 Garching, Germany;* orcid.org/0000-0001-8474-6261

Johanna Plansky − *Functional Nanomaterials Group and Catalysis Research Center, Department of Chemistry, School of Natural Sciences, Technical University of Munich, 85748 Garching, Germany;* orcid.org/0000-0001-5065-5871

Matthias Krinninger − *Functional Nanomaterials Group and Catalysis Research Center, Department of Chemistry, School of Natural Sciences, Technical University of Munich, 85748 Garching, Germany*

Andrey Shavorskiy − *MAX IV Laboratory, Lund University, Lund 221 00, Sweden;* orcid.org/0000-0002-7517-5089

Suyun Zhu − *MAX IV Laboratory, Lund University, Lund 221 00, Sweden*

Ueli Heiz − *Chair of Physical Chemistry and Catalysis Research Center, Department of Chemistry, School of Natural Sciences, Technical University of Munich, 85748 Garching, Germany;* orcid.org/0000-0002-9403-1486

Complete contact information is available at: https://pubs.acs.org/10.1021/acscatal.3c00448

Author Contributions

#S.K. and J.P. contributed equally.

Notes

The authors declare no competing financial interest.

■ ACKNOWLEDGMENTS

This work was funded by the Deutsche Forschungsgemeinschaft (DFG, German Research Foundation) under Germany's Excellence Strategy EXC 2089/1-390776260, through the project CRC1441 (Project Number 426888090), as well as by the grants ES 349/5-2 and HE 3454/23-2. It received funding from the European Research Council (ERC) under the European Union's Horizon 2020 Research and Innovation Program (Grant Agreement No. 850764). B.A.J.L. gratefully acknowledges financial support from the Young Academy of the Bavarian Academy of Sciences and Humanities. The authors acknowledge MAX IV Laboratory for time on HIPPIE Beamline under Proposal 20200272. Research conducted at MAX IV, a Swedish national user facility, is supported by the

Swedish Research council under Contract 2018-07152, the Swedish Governmental Agency for Innovation Systems under Contract 2018-04969, and Formas under Contract 2019-02496.

REFERENCES

(1) Pu, T.; Zhang, W.; Zhu, M. Engineering Heterogeneous Catalysis with Strong Metal−Support Interactions: Characterization, Theory and Manipulation. *Angew. Chem., Int. Ed.* **2023**, *62*, No. e202212278.
(2) Shi, X. Y.; Zhang, W.; Zhang, C.; Zheng, W. T.; Chen, H.; Qi, J. G. Real-space observation of strong metal-support interaction: State-of-the-art and what's the next. *J. Microsc.* **2016**, *262*, 203−215.
(3) Fukamori, Y.; König, M.; Yoon, B.; Wang, B.; Esch, F.; Heiz, U.; Landman, U. Fundamental Insight into the Substrate-Dependent Ripening of Monodisperse Clusters. *ChemCatChem* **2013**, *5*, 3330−3341.
(4) Kim, J.; Choi, H.; Kim, D.; Park, J. Y. Operando Surface Studies on Metal-Oxide Interfaces of Bimetal and Mixed Catalysts. *ACS Catal.* **2021**, *11*, 8645−8677.
(5) Tauster, S. J. Strong Metal-Support Interactions. *Acc. Chem. Res.* **1987**, *20*, 389−394.
(6) Dulub, O.; Hebenstreit, W.; Diebold, U. Imaging Cluster Surfaces with Atomic Resolution: The Strong Metal-Support Interaction State of Pt Supported on TiO_2(110). *Phys. Rev. Lett.* **2000**, *84*, 3646−3649.
(7) Qin, Z. H.; Lewandowski, M.; Sun, Y. N.; Shaikhutdinov, S.; Freund, H. J. Encapsulation of Pt Nanoparticles as a Result of Strong Metal-Support Interaction with Fe_3O_4(111). *J. Phys. Chem. C* **2008**, *112*, 10209−10213.
(8) Lunkenbein, T.; Schumann, J.; Behrens, M.; Schlögl, R.; Willinger, M. G. Formation of a ZnO Overlayer in Industrial Cu/ZnO/Al_2O_3 Catalysts Induced by Strong Metal-Support Interactions. *Angew. Chem.* **2015**, *127*, 4627−4631.
(9) Luo, Z.; Zhao, G.; Pan, H.; Sun, W. Strong Metal−Support Interaction in Heterogeneous Catalysts. *Adv. Energy Mater.* **2022**, *12*, No. 2201395.
(10) Zhu, M.; Tian, P.; Kurtz, R.; Lunkenbein, T.; Xu, J.; Schlögl, R.; Wachs, I. E.; Han, Y. F. Strong Metal−Support Interactions between Copper and Iron Oxide during the High-Temperature Water-Gas Shift Reaction. *Angew. Chem., Int. Ed.* **2019**, *58*, 9083−9087.
(11) Sun, Y. N.; Qin, Z. H.; Lewandowski, M.; Carrasco, E.; Sterrer, M.; Shaikhutdinov, S.; Freund, H. J. Monolayer iron oxide film on platinum promotes low temperature CO oxidation. *J. Catal.* **2009**, *266*, 359−368.
(12) Stühmeier, B. M.; Selve, S.; Patel, M. U. M.; Geppert, T. N.; Gasteiger, H. A.; El-Sayed, H. A. Highly Selective Pt/TiO_x Catalysts for the Hydrogen Oxidation Reaction. *ACS Appl. Energy Mater.* **2019**, *2*, 5534−5539.
(13) Geppert, T. N.; Bosund, M.; Putkonen, M.; Stühmeier, B. M.; Pasanen, A. T.; Heikkilä, P.; Gasteiger, H. A.; El-Sayed, H. A. HOR Activity of Pt-TiO_{2-Y} at Unconventionally High Potentials Explained: The Influence of SMSI on the Electrochemical Behavior of Pt. *J. Electrochem. Soc.* **2020**, *167*, No. 084517.
(14) Xin, H.; Lin, L.; Li, R.; Li, D.; Song, T.; Mu, R.; Fu, Q.; Bao, X. Overturning CO_2 Hydrogenation Selectivity with High Activity via Reaction-Induced Strong Metal-Support Interactions. *J. Am. Chem. Soc.* **2022**, *144*, 4874−4882.
(15) Zhang, Y.; Zhang, Z.; Yang, X.; Wang, R.; Duan, H.; Shen, Z.; Li, L.; Su, Y.; Yang, R.; Zhang, Y.; Su, X.; Huang, Y.; Zhang, T. Tuning selectivity of CO_2 hydrogenation by modulating the strong metal-support interaction over Ir/TiO_2 catalysts. *Green Chem.* **2020**, *22*, 6855−6861.
(16) Li, S.; Xu, Y.; Chen, Y.; Li, W.; Lin, L.; Li, M.; Deng, Y.; Wang, X.; Ge, B.; Yang, C.; Yao, S.; Xie, J.; Li, Y.; Liu, X.; Ma, D. Tuning the Selectivity of Catalytic Carbon Dioxide Hydrogenation over Iridium/Cerium Oxide Catalysts with a Strong Metal−Support Interaction. *Angew. Chem., Int. Ed.* **2017**, *56*, 10761−10765.
(17) Han, G.; Song, H. C.; Kim, S. H.; Park, J. Y. Role of the Support Oxidation State on the Catalytic Activity of Two-Dimensional Pt/TiO_x Catalysts. *J. Phys. Chem. C* **2023**, *127*, 4096−4103.
(18) Petzoldt, P.; Eder, M.; Mackewicz, S.; Blum, M.; Kratky, T.; Günther, S.; Tschurl, M.; Heiz, U.; Lechner, B. A. J. Tuning Strong Metal-Support Interaction Kinetics on Pt-Loaded TiO_2(110) by Choosing the Pressure: A Combined Ultrahigh Vacuum/Near-Ambient Pressure XPS Study. *J. Phys. Chem. C* **2022**, *126*, 16127−16139.
(19) Frey, H.; Beck, A.; Huang, X.; van Bokhoven, J. A.; Willinger, M. G. Dynamic interplay between metal nanoparticles and oxide support under redox conditions. *Science* **2022**, *376*, 982−987.
(20) Kraushofer, F.; Parkinson, G. S. Single-Atom Catalysis: Insights from Model Systems. *Chem. Rev.* **2022**, *122*, 14911−14939.
(21) Fu, Q.; Saltsburg, H.; Flytzani-Stephanopoulos, M. Active Nonmetallic Au and Pt Species on Ceria-Based Water-Gas Shift Catalysts. *Science* **2003**, *301*, 935−938.
(22) Xie, S.; Liu, L.; Lu, Y.; Wang, C.; Cao, S.; Diao, W.; Deng, J.; Tan, W.; Ma, L.; Ehrlich, S. N.; Li, Y.; Zhang, Y.; Ye, K.; Xin, H.; Flytzani-Stephanopoulos, M.; Liu, F. Pt Atomic Single-Layer Catalyst Embedded in Defect-Enriched Ceria for Efficient CO Oxidation. *J. Am. Chem. Soc.* **2022**, *144*, 21255−21266.
(23) Maurer, F.; Jelic, J.; Wang, J.; Gänzler, A.; Dolcet, P.; Wöll, C.; Wang, Y.; Studt, F.; Casapu, M.; Grunwaldt, J. D. Tracking the formation, fate and consequence for catalytic activity of Pt single sites on CeO_2. *Nat. Catal.* **2020**, *3*, 824−833.
(24) Crampton, A. S.; Rotzer, M. D.; Landman, U.; Heiz, U. Can Support Acidity Predict Sub-Nanometer Catalyst Activity Trends? *ACS Catal.* **2017**, *7*, 6738−6744.
(25) Beniya, A.; Higashi, S.; Ohba, N.; Jinnouchi, R.; Hirata, H.; Watanabe, Y. CO Oxidation Activity of Non-Reducible Oxide-Supported Mass-Selected Few-Atom Pt Single-Clusters. *Nat. Commun.* **2020**, *11*, No. 1888.
(26) Ostwald, W. Über die vermeintliche Isomerie des roten und gelben Quecksilberoxyds und die Oberflächenspannung fester Körper. *Z. Phys. Chem.* **1900**, *34U*, 495−503.
(27) Smoluchowski, M. Drei Vorträge über Diffusion, brownsche Bewegung und Koagulation von Kolloidteilchen. *Z. Phys. Chem.* **1916**, *17*, 557−585.
(28) Hu, K. J.; Plant, S. R.; Ellis, P. R.; Brown, C. M.; Bishop, P. T.; Palmer, R. E. Atomic Resolution Observation of a Size-Dependent Change in the Ripening Modes of Mass-Selected Au Nanoclusters Involved in CO Oxidation. *J. Am. Chem. Soc.* **2015**, *137*, 15161−15168.
(29) Hansen, T. W.; Delariva, A. T.; Challa, S. R.; Datye, A. K. Sintering of Catalytic Nanoparticles: Particle Migration or Ostwald Ripening? *Acc. Chem. Res.* **2013**, *46*, 1720−1730.
(30) Moulijn, J. A.; van Diepen, A. E.; Kapteijn, F. Catalyst deactivation: Is it predictable? What to do? *Appl. Catal., A* **2010**, *32*, 3−16.
(31) Argyle, M. D.; Bartholomew, C. H. Heterogeneous Catalyst Deactivation and Regeneration: A Review. *Catalysts* **2015**, *5*, 145−269.
(32) Wan, Q.; Hu, S.; Dai, J.; Chen, C.; Li, W. X. First-Principles Kinetic Study for Ostwald Ripening of Late Transition Metals on TiO_2(110). *J. Phys. Chem. C* **2019**, *123*, 1160−1169.
(33) Li, Z.; Chen, H. Y. T.; Schouteden, K.; Picot, T.; Liao, T. W.; Seliverstov, A.; van Haesendonck, C.; Pacchioni, G.; Janssens, E.; Lievens, P. Unraveling the atomic structure, ripening behavior, and electronic structure of supported Au_{20} clusters. *Sci. Adv.* **2020**, *6*, No. eaay4289.
(34) Su, Y. Q.; Liu, J. X.; Filot, I. A. W.; Hensen, E. J. M. Theoretical Study of Ripening Mechanisms of Pd Clusters on Ceria. *Chem. Mater.* **2017**, *29*, 9456−9462.
(35) Wettergren, K.; Schweinberger, F. F.; Deiana, D.; Ridge, C. J.; Crampton, A. S.; Rötzer, M. D.; Hansen, T. W.; Zhdanov, V. P.; Heiz, U.; Langhammer, C. High Sintering Resistance of Size-Selected

https://doi.org/10.1021/acscatal.3c00448
ACS Catal. 2023, 13, 6203−6213

Platinum Cluster Catalysts by Suppressed Ostwald Ripening. *Nano Lett.* **2014**, *14*, 5803−5809.
(36) Zandkarimi, B.; Poths, P.; Alexandrova, A. N. When Fluxionality Beats Size Selection: Acceleration of Ostwald Ripening of Sub-Nano Clusters. *Angew. Chem., Int. Ed.* **2021**, *60*, 11973−11982.
(37) Zandkarimi, B.; Gorey, T. J.; Li, G.; Munarriz, J.; Anderson, S. L.; Alexandrova, A. N. Alloying with Sn Suppresses Sintering of Size-Selected Subnano Pt Clusters on SiO_2 with and without Adsorbates. *Chem. Mater.* **2020**, *32*, 8595−8605.
(38) Niu, Y.; Schlexer, P.; Sebok, B.; Chorkendorff, I.; Pacchioni, G.; Palmer, R. E. Reduced Sintering of Mass-Selected Au Clusters on SiO_2 by Alloying with Ti: An Aberration-Corrected STEM and Computational Study. *Nanoscale* **2018**, *10*, 2363−2370.
(39) Yin, P.; Hu, S.; Qian, K.; Wei, Z.; Zhang, L.; Lin, Y.; Huang, W.; Xiong, H.; Li, W. X.; Liang, H. W. Quantification of critical particle distance for mitigating catalyst sintering. *Nat. Commun.* **2021**, *12*, No. 4865.
(40) Jiang, Y.; Zhu, Y.; Zhou, D.; Jiang, Z.; Si, N.; Stacchiola, D.; Niu, T. Reversible oxidation and reduction of gold-supported iron oxide islands at room temperature. *J. Chem. Phys.* **2020**, *152*, No. 074710.
(41) Fleet, M. E. The Structure of Magnetite. *Acta Crystallogr., Sect. B* **1981**, *37*, 917−920.
(42) Verwey, E. J. W.; Heilmann, E. L. Physical Properties and Cation Arrangement of Oxides with Spinel Structures I. Cation Arrangement in Spinels. *J. Chem. Phys.* **1947**, *15*, 174−180.
(43) Verwey, E. J.; Haayman, P. W.; Romeijn, F. C. Physical Properties and Cation Arrangement of Oxides with Spinel Structures II. Electronic Conductivity. *J. Chem. Phys.* **1947**, *15*, 181−187.
(44) Bliem, R.; Mcdermott, E.; Ferstl, P.; Setvin, M.; Gamba, O.; Pavelec, J.; Schneider, M. A.; Schmid, M.; Diebold, U.; Blaha, P.; Hammer, L.; Parkinson, G. S. Subsurface cation vacancy stabilization of the magnetite (001) surface. *Science* **2014**, *346*, 1215−1218.
(45) Parkinson, G. S.; Novotný, Z.; Jacobson, P.; Schmid, M.; Diebold, U. A Metastable Fe(A) Termination at the Fe3O4(001) Surface. *Surf. Sci.* **2011**, *605*, L42−L45.
(46) Parkinson, G. S. Iron Oxide Surfaces. *Surf. Sci. Rep.* **2016**, *71*, 272−365.
(47) Parkinson, G. S.; Manz, T. A.; Novotný, Z.; Sprunger, P. T.; Kurtz, R. L.; Schmid, M.; Sholl, D. S.; Diebold, U. Antiphase domain boundaries at the $Fe_3O_4(001)$ surface. *Phys. Rev. B* **2012**, *85*, No. 195450.
(48) Bourgund, A.; Lechner, B. A. J.; Meier, M.; Franchini, C.; Parkinson, G. S.; Heiz, U.; Esch, F. Influence of Local Defects on the Dynamics of O−H Bond Breaking and Formation on a Magnetite Surface. *J. Phys. Chem. C* **2019**, *123*, 19742−19747.
(49) Gamba, O.; Hulva, J.; Pavelec, J.; Bliem, R.; Schmid, M.; Diebold, U.; Parkinson, G. S. The Role of Surface Defects in the Adsorption of Methanol on $Fe_3O_4(001)$. *Top. Catal.* **2017**, *60*, 420−430.
(50) Hulva, J.; Jakub, Z.; Novotny, Z.; Johansson, N.; Knudsen, J.; Schnadt, J.; Schmid, M.; Diebold, U.; Parkinson, G. S. Adsorption of CO on the $Fe_3O_4(001)$ Surface. *J. Phys. Chem. B* **2018**, *122*, 721−729.
(51) Meier, M.; Hulva, J.; Jakub, Z.; Pavelec, J.; Setvin, M.; Bliem, R.; Schmid, M.; Diebold, U.; Franchini, C.; Parkinson, G. S. Water Agglomerates on $Fe_3O_4(001)$. *Proc. Natl. Acad. Sci. U.S.A.* **2018**, *115*, E5642−E5650.
(52) Marcinkowski, M. D.; Yuk, S. F.; Doudin, N.; Smith, R. S.; Nguyen, M. T.; Kay, B. D.; Glezakou, V. A.; Rousseau, R.; Dohnálek, Z. Low-Temperature Oxidation of Methanol to Formaldehyde on a Model Single-Atom Catalyst: Pd Atoms on $Fe_3O_4(001)$. *ACS Catal.* **2019**, *9*, 10977−10982.
(53) Kaiser, S.; Maleki, F.; Zhang, K.; Harbich, W.; Heiz, U.; Tosoni, S.; Lechner, B. A. J.; Pacchioni, G.; Esch, F. Cluster Catalysis with Lattice Oxygen: Tracing Oxygen Transport from a Magnetite (001) Support onto Small Pt Clusters. *ACS Catal.* **2021**, *11*, 9519−9529.
(54) Heiz, U.; Vanolli, F.; Trento, L.; Schneider, W. D. Chemical reactivity of size-selected supported clusters: An experimental setup. *Rev. Sci. Instrum.* **1997**, *68*, 1986−1994.
(55) Bonanni, S.; Aït-Mansour, K.; Hugentobler, M.; Brune, H.; Harbich, W. An experimental setup combining a highly sensitive detector for reaction products with a mass-selected cluster source and a low-temperature STM for advanced nanocatalysis. *Eur. Phys. J. D* **2011**, *63*, 241−249.
(56) Nečas, D.; Klapetek, P. Gwyddion: An open-source software for SPM data analysis. *Cent. Eur. J. Phys.* **2012**, *10*, 181−188.
(57) Zhu, S.; Scardamaglia, M.; Kundsen, J.; Sankari, R.; Tarawneh, H.; Temperton, R.; Pickworth, L.; Cavalca, F.; Wang, C.; Tissot, H.; Weissenrieder, J.; Hagman, B.; Gustafson, J.; Kaya, S.; Lindgren, F.; Kallquist, I.; Maibach, J.; Hahlin, M.; Boix, V.; Gallo, T.; Rehman, F.; D'Acunto, G.; Schnadta, J.; Shavorskiy, A. HIPPIE: A New Platform for Ambient-Pressure X-Ray Photoelectron Spectroscopy at the MAX IV Laboratory. *J. Synchrotron Radiat.* **2021**, *28*, 624−636.
(58) Shimizu, S.; Noritake, H.; Koitaya, T.; Mukai, K.; Yoshimoto, S.; Yoshinobu, J. Site-specific chemical states of adsorbed CO on Pt(997): A high resolution XPS study. *Surf. Sci.* **2013**, *608*, 220−225.
(59) Toyoshima, R.; Yoshida, M.; Monya, Y.; Suzuki, K.; Amemiya, K.; Mase, K.; Mun, B. S.; Kondoh, H. A high-pressure-induced dense CO overlayer on a Pt(111) surface: A chemical analysis using in situ near ambient pressure XPS. *Phys. Chem. Chem. Phys.* **2014**, *16*, 23564−23567.
(60) Libra, J. *KolXPD: Spectroscopy Data Measurement and Processing*, 2015.
(61) Whitman, L. J.; Richter, L. J.; Gurney, B. A.; Villarrubia, J. S.; Ho, W. Co adsorption site occupations on Fe(111) vs coverage and temperature: The kinetics of adsorption and reaction. *J. Chem. Phys.* **1989**, *90*, 2050−2062.
(62) Kelemen, S. R.; Kaldor, A.; Dwyer, D. J. The Adsorption of CO on Clean and Potassium Promoted FeO Surfaces. *Surf. Sci.* **1982**, *121*, 45−60.
(63) Zhang, K.; Shaikhutdinov, S.; Freund, H.-J. Does the Surface Structure of Oxide Affect the Strong Metal-Support Interaction with Platinum? Platinum on $Fe_3O_4(001)$ versus $Fe_3O_4(111)$. *ChemCatChem* **2015**, *7*, 3725−3730.
(64) Arndt, B.; Lechner, B. A. J.; Bourgund, A.; Grånäs, E.; Creutzburg, M.; Krausert, K.; Hulva, J.; Parkinson, G. S.; Schmid, M.; Vonk, V.; Esch, F.; Stierle, A. Order-disorder phase transition of the subsurface cation vacancy reconstruction on $Fe_3O_4(001)$. *Phys. Chem. Chem. Phys.* **2020**, *22*, 8336−8343.
(65) Bliem, R.; Van Der Hoeven, J.; Zavodny, A.; Gamba, O.; Pavelec, J.; De Jongh, P. E.; Schmid, M.; Diebold, U.; Parkinson, G. S. An Atomic-Scale View of CO and H_2 Oxidation on a Pt/Fe_3O_4 Model Catalyst Angewandte. *Angew. Chem.* **2015**, *127*, 13999−14002.
(66) Novotny, Z.; Mulakaluri, N.; Edes, Z.; Schmid, M.; Pentcheva, R.; Diebold, U.; Parkinson, G. S. Probing the surface phase diagram of $Fe_3O_4(001)$ towards the Fe-rich limit: Evidence for progressive reduction of the Surface. *Phys. Rev. B* **2013**, *87*, No. 195410.
(67) Bliem, R.; van der Hoeven, J. E. S.; Hulva, J.; Pavelec, J.; Gamba, O.; de Jongh, P. E.; Schmid, M.; Blaha, P.; Diebold, U.; Parkinson, G. S. Dual Role of CO in the Stability of Subnano Pt Clusters at the Fe_3O_4 (001) Surface. *Proc. Natl. Acad. Sci. U.S.A.* **2016**, *113*, 8921−8926.
(68) The encapsulating layer thickness was calculated based on the Pt 4f signal attenuation.[69] Using a density of 5.9 g/cm^3,[46] and a band gap of 2.1 eV,[70] the electron inelastic mean free path for a nominal FeO layer was calculated to be 7.22 Å for 307 eV and 16.78 Å for 921 eV photon energy.[71]
(69) Riviere, J. C.; Myhra, S. *Handbook of Surface and Interface Analysis: Methods for Problem-Solving.*; CRC Press, 2009; p 237.
(70) Di Sabatino, S.; Koskelo, J.; Berger, J. A.; Romaniello, P. Photoemission spectrum in paramagnetic FeO under pressure: Towards an ab initio description. *Phys. Rev. Res.* **2021**, *3*, No. 013172.
(71) Tanuma, S.; Penn, D. R. Calculations of Electron Inelastic Mean Free Paths. *Surf. Interface Anal.* **1993**, *20*, 77−89.
(72) Ritter, M.; Ranke, W.; Weiss, W. Growth and structure of ultrathin FeO films on Pt(111) studied by STM and LEED. *Phys. Rev. B* **1998**, *57*, 7240−7251.

https://doi.org/10.1021/acscatal.3c00448
ACS Catal. 2023, 13, 6203−6213

(73) Lewandowski, M.; Sun, Y. N.; Qin, Z. H.; Shaikhutdinov, S.; Freund, H. J. Promotional effect of metal encapsulation on reactivity of iron oxide supported Pt catalysts. *Appl. Catal., A* **2011**, *391*, 407−410.
(74) Yamashita, T.; Hayes, P. Analysis of XPS spectra of Fe^{2+} and Fe^{3+} ions in oxide materials. *Appl. Surf. Sci.* **2008**, *254*, 2441−2449.
(75) Bagus, P. S.; Nelin, C. J.; Brundle, C. R.; Crist, B. V.; Lahiri, N.; Rosso, K. M. Combined multiplet theory and experiment for the Fe2p and 3p XPS of FeO and Fe_2O_3. *J. Chem. Phys.* **2021**, *154*, No. 094709.
(76) Krupski, K.; Moors, M.; Jóźwik, P.; Kobiela, T.; Krupski, A. Structure Determination of Au on Pt(111) Surface: LEED, STM and DFT Study. *Materials* **2015**, *8*, 2935−2952.

https://doi.org/10.1021/acscatal.3c00448
ACS Catal. 2023, 13, 6203−6213